Spatial distribution of glacial erosion rates in the St. Elias range, Alaska, inferred from a realistic model of glacier dynamics

Rachel Headley,[1,2] Bernard Hallet,[1] Gerard Roe,[1] Edwin D. Waddington,[1] and Eric Rignot[3,4]

Received 29 November 2011; revised 29 June 2012; accepted 11 July 2012; published 8 September 2012.

[1] Glaciers have been principal erosional agents in many orogens throughout much of the recent geological past. A modern example is the St. Elias Mountains in southeastern Alaska; it is a highly convergent, complex orogen, which has been glaciated for much of its history. We examine the Seward-Malaspina Glacier system, which comprises two of the largest temperate glaciers in the world. We focus on the pattern of erosion within its narrow passage through the St. Elias Mountains, the Seward Throat. Measured glacier surface velocities and elevations provide constraints for a full-stress numerical flowband model that enables us to quantitatively determine the glacier thickness profile, which is not easily measured on temperate glaciers, and the basal characteristics relevant for erosion. These characteristics at the bed, namely the water pressure, normal and shear stresses, and sliding velocity, are then used to infer the spatial variation in erosion rates using several commonly invoked erosion laws. The calculations show that the geometry of the glacier basin exerts a far stronger control on the spatial variation of erosion rates than does the equilibrium line altitude, which is often assumed to be important in studies of glaciated orogens. The model provides a quantitative basis for understanding why erosion rates are highest around the Seward Throat, which is generally consistent with local and large-scale geological observations and thermochronologic evidence. Moreover, model results suggest how glacier characteristics could be used to infer zones of active or recent uplift in ice-mantled orogens.

Citation: Headley, R., B. Hallet, G. Roe, E. D. Waddington, and E. Rignot (2012), Spatial distribution of glacial erosion rates in the St. Elias range, Alaska, inferred from a realistic model of glacier dynamics, *J. Geophys. Res.*, *117*, F03027, doi:10.1029/2011JF002291.

1. Introduction

[2] The interactions among surface processes, climate, and tectonics in active orogens have been at the forefront of Earth science research in recent decades [e.g., *Molnar and England*, 1990; *Beaumont et al.*, 1992; *Koons*, 1995; *Zeitler et al.*, 2001; *Wobus et al.*, 2003; *Bookhagen et al.*, 2005]. There is considerable interest in glacial erosion in tectonically active mountain ranges [e.g., *Tomkin and Braun*, 2002; *Herman and Braun*, 2008; *Yanites and Ehlers*, 2012] because erosion by temperate glaciers, especially those in Alaska, can be exceptionally fast and tends to be an important or dominant exhumation agent in active orogens through the Quaternary [*Hallet*, 1996; *Delmas et al.*, 2009; *Koppes and Montgomery*, 2009]. While modeling the role of glaciers in orogenic development has yielded useful insights [*Tomkin*, 2007; *Herman and Braun*, 2008], much is to be learned from glaciologically focused studies of currently glaciated, tectonically active regions.

[3] The St. Elias Mountains constitute a prime example of an active, compressional orogen being impacted by climate, through the erosion by the large glaciers in the region [e.g., *Meigs and Sauber*, 2000; *Spotila et al.*, 2004]. The large-scale patterns (both temporal and spatial) of tectonic development, exhumation, and sedimentation have been identified through diverse studies of the structural geology, thermochronology, and offshore geophysics [*Jaeger et al.*, 1998; *Bruhn et al.*, 2004; *Berger et al.*, 2008; *Chapman et al.*, 2008; *Enkelmann et al.*, 2010]. Across the glaciers in southern Alaska, recent basin-averaged erosion rates have been estimated from glacier sediment output [*Humphrey and Raymond*, 1994; *Hallet*, 1996; *Koppes and Hallet*, 2006] and

[1]Department of Earth and Space Sciences, University of Washington, Seattle, Washington, USA.
[2]Now at Institut für Geowissenschaften, Universität Tübingen, Tübingen, Germany.
[3]Department of Earth System Science, University of California, Irvine, California, USA.
[4]Jet Propulsion Laboratory, California Institute of Technology, Pasadena, California, USA.

Corresponding author: R. Headley, Institut für Geowissenschaften, Universität Tübingen, Wilhelmstrasse 56, D-72074 Tübingen, Germany. (rheadley@u.washington.edu)

0148-0227/12/2011JF002291

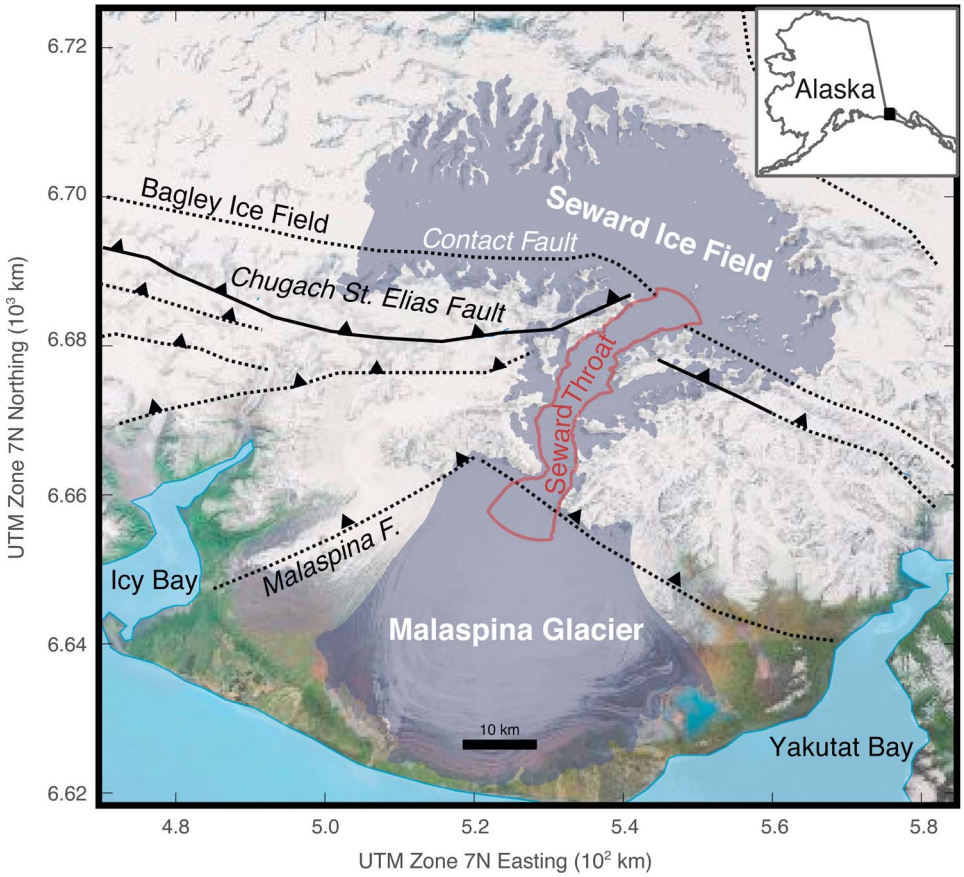

Figure 1. Entire Seward-Malaspina glacier system; inset shows location in Alaska. The Seward Throat is outlined in red. The major faults are labeled in italics, including the principal thrust faults, the Chugach St. Elias fault and the Malaspina fault [*Enkelmann et al.*, 2008].

offshore sediment volumes [*Jaeger et al.*, 1998; *Sheaf et al.*, 2003]. While large-scale exhumation patterns and basin-averaged erosion rates are informative of the dynamics of the orogen, details of how the erosion rate varies over the landscape requires a closer look at specific glaciers.

[4] We consider an exceptionally fast-moving portion of one the region's principal glacier systems, the Seward Throat of the Seward-Malaspina system. This work capitalizes on empirical data available for this glacier and uses a 2D full-stress numerical model of glacier flow to define the spatial variability of the ice thickness and basal characteristics. While we focus on a specific glacier, the method could be used on any glacier for which sufficient data exist to constrain the model. For many temperate glaciers, the ice thickness and basal properties are not easily measured. Over the Seward Throat, airborne radar measurements of glacier thickness have been largely unsuccessful because the glacier is thick and heavily crevassed. We start off by determining the ice thickness using the numerical model constrained by observed surface velocities and elevations. We then calculate the basal characteristics relevant for erosion, including the sliding velocity, water pressure, and normal and shear stresses. From these properties, we infer the spatial variation in erosion rates and discuss it in the context of empirical data defining the spatial variation of rates of exhumation and crustal deformation in the region.

2. Setting

2.1. Glaciological Setting

[5] The Seward-Malaspina Glacier system is in southeastern coastal Alaska and extends into the southwestern corner of the Yukon Territory in Canada, east of Mt. St. Elias (Figure 1). It covers around 3900 km^2 and originates in the Saint Elias Mountains and on the Mount Logan massif, where peaks exceed 5500 m above sea level and precipitation is high. The nearest long-term meteorological measurements are from Yakutat, a coastal town around 40 km to the SE and across Yakutat Bay; the annual precipitation and temperature average 5 m and 4°C, respectively (http://www.wrcc.dri.edu/summary/yak.ak.html; accessed November 2008). From the Seward Ice Field, which is an accumulation area exceeding 60 km in width, the ice funnels through the mountains in a 4–6 km wide passage, which drops steeply from approximately 1500 m to 600 m above sea level (Figure 1). This narrow passage, the Seward Throat, is the focus of this paper. South of the Seward Throat, the glacier spreads out in a large piedmont lobe, forming the main portion of Malaspina

Glacier. This lobe is also fed from the west by Agassiz Glacier and from the east by several smaller glaciers. The distinctive piedmont lobe of Malaspina Glacier has been extensively investigated [e.g., *Sharp*, 1951; *Allen and Smith*, 1953; *Ford et al.*, 2003], while the Seward Throat has received considerably less attention due largely to the ruggedness and inaccessibility of the terrain.

[6] Glacial coverage has been continuous in the St. Elias Mountains from the Pliocene to the present [*Péwé*, 1975]. Offshore sediments indicate that Malaspina Glacier was likely a tidewater glacier that extended perhaps 100 km onto the continental shelf at the Last Glacial Maximum [*Molnia*, 1986; W. F. Manley and D. S. Kaufman, Alaska PaleoGlacier Atlas: Institute of Arctic and Alpine Research: A Geospatial Compilation of Pleistocene Glacier Extents, 2002, http://instaar.colorado.edu/QGISL/ak_paleoglacier_atlas/, hereinafter referred to as Manley and Kaufman, online data, 2002]. While there is currently little or no calving, for the last century Malaspina Glacier has terminated at or near the Pacific coast [*Porter*, 1989].

[7] This region is one of few where orogen-scale and basin-averaged glacial erosion rates have been extensively studied. Averaged over the length of the entire St. Elias range, offshore sedimentation rates imply erosion rates of 5.1 mm yr^{-1} for the past 10^4 years [*Sheaf et al.*, 2003] and similar rates for the last century [*Jaeger et al.*, 1998]. The basin-wide erosion rate has been estimated for glaciers adjacent to, and within similar climatic and structural settings as, the Seward-Malaspina system. This rate averages over 9 mm yr^{-1} for Tyndall Glacier in Icy Bay over the last centuries [*Koppes and Hallet*, 2006] and around 11 mm yr^{-1} for Hubbard Glacier [*Trusel et al.*, 2008].

2.2. Geological Setting

[8] This region's glaciological and geological histories are tightly intertwined, with evidence (particularly ice-rafted debris in the Pacific) of syn-collisional glacier cover and erosion starting as early as 5.6 Ma [*Plafker*, 1987; *Lagoe et al.*, 1993; *Plafker et al.*, 1994]. The tectonic setting of the Seward-Malaspina system has been dominated by convergence between the Yakutat terrane and North America since 5–10 Ma [*Plafker et al.*, 1994; *Meigs et al.*, 2008]. Many major faults traverse this region, including the Chugach St. Elias thrust fault and Contact Fault, which is completely under glacial cover (Figure 1) but can be been inferred from geodetic measurements, structural analysis of the surrounding region, and geological observations on isolated nunataks [e.g., *Bruhn et al.*, 2004; *Chapman et al.*, 2008; *Elliott et al.*, 2010]. The Seward and Malaspina glaciers cover many of these major faults and associated ancillary structures, both active and inactive (Figure 1).

[9] Currently, geodetic studies show overall NW-SE crustal convergence between the Yakutat Block and southern Alaska; 37 mm yr^{-1} of convergence occurs mainly between the coast and the Bagley and Seward Ice Fields, a distance of around 70 km [*Elliott et al.*, 2010; *Elliott*, 2011]. For comparison, the corresponding strain rate, assuming a conservative estimate of 20 mm yr^{-1} across the 70 km distance, is slightly higher than that occurring in the Himalaya, which is 15−20 mm yr^{-1} [*Zhang et al.*, 2004] over a distance of about 100 km. Seismic studies of the St. Elias range are consistent with geodetic observations and also highlight a region of enhanced activity situated between the coast and ice fields [*Pavlis et al.*, 2008]. Thus, the Seward Throat cuts across a zone of exceptionally active crustal convergence, where rapid and variable rock uplift is expected and is reflected in the extreme topography, including Mt. St. Elias, the third highest peak in North America.

2.3. Data Coverage

[10] Over the past decade, satellite and airborne instruments have provided invaluable surface-elevation, thickness, and velocity measurements for many ice masses, including the Seward-Malaspina system. Here we use high-resolution digital elevation models (DEMs) of the ice and surrounding region derived from the Shuttle Radar Topography Mission (SRTM) measurements; they were acquired during winter 2000, at 30 m resolution over most of the glacier system, with vertical accuracy of about 16 m [*Muskett et al.*, 2008]. Part of the accumulation area lies above 60.5°N, where there is no SRTM coverage, but this portion is not considered in this work. While the surface elevation of Malaspina Glacier can change rapidly from both surging [*Muskett et al.*, 2008] and mass loss due to a warming climate [*Sauber et al.*, 2005], the ice surface through the Seward Throat appears to have lowered fairly uniformly by less than a few meters since 2000 based on comparisons of the SRTM measurements with more recent airborne laser profiles [*Arendt et al.*, 2008].

[11] Compared to the elevation of the ice surface, the glacier thickness in the study region is essentially unknown. *Conway et al.* [2009] conducted an airborne ice-penetrating radar survey, in 2005, to determine glacier thicknesses in the region. The measurements were successful over sections of Malaspina Glacier but not through the Seward Throat, likely due to severe surface crevassing [*Conway et al.*, 2009]. However, these measurements still provide important constraints for determining the ice thickness, as described below. Uncertainties for these ice thickness measurements are small, generally less than 18 m [*Conway et al.*, 2009].

[12] In contrast to the ice thickness, high-resolution surface velocity measurements are available and are presented in Figure 2. The data used to generate this velocity map (Figure 2) were acquired by the Canadian Space Agency's RADARSAT-1 synthetic aperture radar, which operates at C-band frequency (5.6 GHz), with horizontal transmit and receive polarization. We combined orbits 25333 and 25676 acquired in fine beam mode F1 on, respectively, 9/11/2000 and 10/5/2000, i.e., 24 days apart. The data were processed using a speckle tracking algorithm [*Michel and Rignot*, 1999] and assuming surface parallel flow to obtain a three-dimensional vector of ice flow. The data effectively represent the average speed of the ice over a 24-day period. SRTM is used for topographic control. The pixel spacing of the radar data is 7.5 m on the ground in the radar-looking direction, and 6.1 m in the along track direction. Measurement noise is nominally about 1/100th of a pixel, which is equivalent to approximately 1 m yr^{-1}. In practice, the velocity measurements have a precision of a few meters per year, which is small compared to the speed of the glacier (1 km yr^{-1}). Good measurements are obtained in the Seward Throat. Data quality degrades on the Malaspina lobe due to rapid surface melting, and in the upper reaches of the glacier due to surface weathering and lower signal-to-noise ratio.

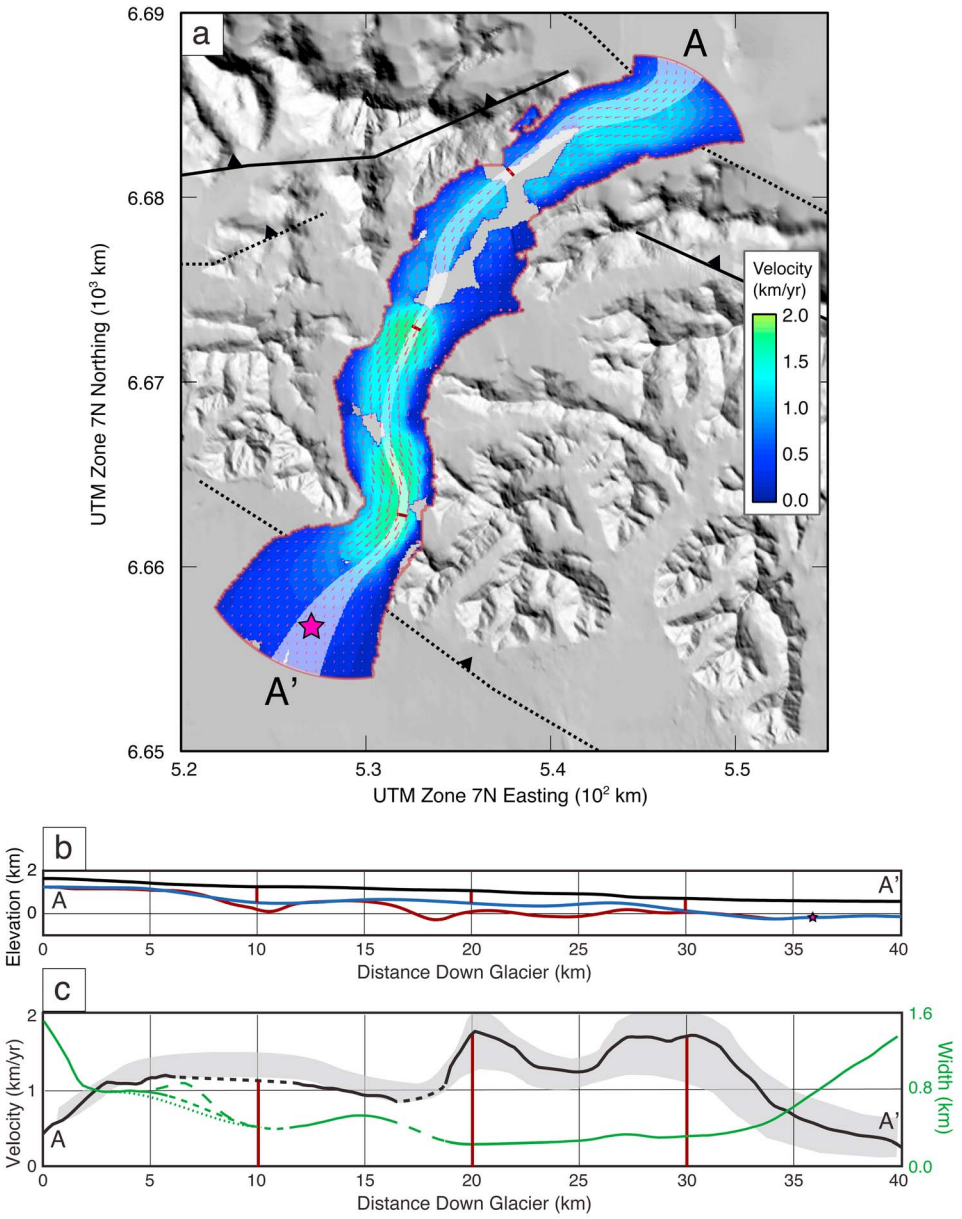

Figure 2. (a) The Seward Throat surface velocities and flow vectors (section 2.3). The maximum velocities approach 2 km yr^{-1}. The flowband, defined by the flow vectors, used in the analysis is highlighted in white. Ice thickness was measured at the pink star. (b) Surface profile (black line) and bed profiles (blue and red lines), with no vertical exaggeration. Red line is the initial bed found from simple mass conservation (equation (1)) and shallow-ice approximations; the blue line is the best fit bed using the full-stress model constrained by measured surface topography and velocity. Red vertical bars correspond to the red flowband gates in Figure 2a. (c) Measured surface velocity in black (left axis; dashed where observations were missing and have been interpolated). The standard deviation of the mean velocity is less than 10% over the profile. Range of seasonal and inter-annual variation over a few years is shown in light gray based on *Burgess et al.* [2010]. Flowband widths are shown in green (right axis). In the 5-to-10 km reach near the entrance of the Throat, where insufficient velocity data exist to constrain the width, three interpolations are shown: the flowband shown in Figure 4a (long-dashes), spline fit between 6 and 11 km (short-dashes), and a spline fit between 3 and 11 km (dots).

[13] As ice funnels from the Seward Ice Field through the Seward Throat, surface velocities increase, over tens of kilometers, from less than 0.5 km yr^{-1} to over 1.8 km yr^{-1} (Figure 2). Point measurements of surface velocity in the lower section of the Seward Throat made by Austin Post in the summer of 1971 (unpublished) and by *Headley et al.* [2007] in the summer of 2007 are similar, suggesting that the overall spatial pattern of surface velocity is stable over at least a few decades. Because mass balance has little

influence on flow through the Seward Throat, as discussed in Section 3.1, surface elevation is controlled primarily by the ice flux entering from the ice field above. Using this assumption, to transit the 40 km length of the Seward Throat at an average speed of 1 km yr^{-1} takes about 40 years, which can be interpreted as a characteristic time to change the surface elevation. Since observations are available from over 40 years ago, we determine that large but slow thickness changes are not ongoing. Although the overall pattern is fairly robust, annual and seasonal variations in speed do occur. *Burgess et al.* [2010] found such variations in the surface velocity, with the largest variation near the surface velocity peaks around down-glacier distances 20 km and 27–31 km (Figure 2c). Temporal changes in subglacial hydrology are the most likely causes for these velocity variations [e.g., *Gordon et al.*, 1998; *Harper et al.*, 2005]. The sensitivity of the modeled basal sliding to the basal water pressure is explored in Section 3.4. Despite these variations, however, the overall observed spatial distribution of velocity is robust and provides a sound empirical basis for defining the bed by estimating ice thickness.

3. Determining the Bed Topography

[14] The glacier thickness is addressed along a two-dimensional section (Figure 2) defined by a flowband extending down the center of the Seward Throat. To minimize sidewall effects and define a region of conserved ice flow, the boundaries of this flowband (Figure 2a) are inferred from flow lines defined by the InSAR surface velocity vectors, which are interpolated on a 50 m by 50 m grid. In order to minimize the effects of uncertainty in any given vector, the minimum width of the flowband has been chosen to be around an order of magnitude larger than this grid spacing. This width ranges from about 0.3 to 1.4 km (Figure 2c). Because the velocities in the reach between 6 and 11 km are poorly defined, uncertainties in the width of the flow band in this region are significantly larger than for the rest of the Seward Throat; the width through this reach is inferred using a smooth function to interpolate the velocities (Figure 2c shows three possibilities). For the remainder of the analysis, we use the velocity, and elevations of the ice surface and of the bed averaged across this single, central flowband (Figures 2b and 2c).

[15] In order to find the ice thickness, the following steps are undertaken: Initial estimates for the glacier thickness are found using a simple mass conservation method. The bed from this method is then evaluated within a 2D full-stress glacier flow line model, and considerable discrepancies between observed and modeled surface velocities are found over a large section of the Seward Throat. Finally, we refine the calculated bed elevation to provide a closer match between measured surface velocities and values modeled using the full stress model.

3.1. Initial Thickness Estimate

[16] For other large Alaskan glaciers, a mass conservation method based upon the shallow ice approximation (SIA) has been used to find the ice thickness [e.g., *Rasmussen*, 1989; *O'Neel et al.*, 2005]. The SIA neglects the effects of the longitudinal stresses relative to the shear stresses, so that ice motion is dependent only upon local topographic effects [*Paterson*, 1994], and the mass conservation method assumes that the ice flux and the surface velocity are defined at all points along the glacier. The ice flux is the product of ice thickness H, the flow-band width, W, and $\bar{u}$, the depth-averaged velocity, which can be related to the surface velocity (u_{surf}) by $\bar{u} = \alpha\, u_{surf}$. The flux is thus defined by $F = \alpha\, u_{surf} HW$. For the shallow ice approximation, α with a value of 0.8 represents only deformation with no sliding, and α with a value of 1.0 is all sliding. Empirical values of α of 0.8 or more are not uncommon for fast-moving, temperate glaciers [*Paterson*, 1994, p. 135].

[17] For the Seward Throat, the flux can be defined where x_0 = 36 km along the glacier length (Figure 2), where radar measurements [*Conway et al.*, 2009] define the ice thickness: $H(x_0)$ = 800 m. Following *O'Neel et al.* [2005], we assume that α does not vary spatially in this initial estimate of the thickness, so that α cancels out when comparing the flux between any two locations. With the additional assumption that the flux is spatially uniform, the thickness as a function of distance downglacier can be estimated from:

$$H(x) = \frac{H(x_0)W(x_0)u_{surf}(x_0)}{W(x)u_{surf}(x)}, \tag{1}$$

where $u_{surf}(x)$ is based on the satellite radar measurements and $W(x)$ is determined from the local width of the chosen flowband (Figures 2a and 2c). The small effect of ice loss due to ablation on the ice flux through this short reach is neglected in this calculation, though it could be readily incorporated [e.g., *O'Neel et al.*, 2005]. Mass balance observations in the region are sparse [*Sharp*, 1951; *Meier and Post*, 1962; *Tangborn*, 1999]. Assuming a liberal 2 m yr^{-1} of ablation over the 40 km length of the Seward Throat, the mass balance accounts for a loss of 8×10^4 m^2 yr^{-1} averaged over the width, compared to a conservative width-averaged average flux of 8×10^5 m^2 yr^{-1} from 800 m thick ice moving at 1 km yr^{-1}. From this calculation, ablational loss through the Seward Throat is around 10% of the ice flux and is thus considered negligible in this context.

[18] Using equation (1), we calculate the ice thickness along the flowband at uniform distance increments of 200 m. The 18 m uncertainty in the thickness measurement has a negligible (less than 2%) effect on the calculated thickness profile. We solve for thickness at each point locally using equation (1), so that transient effects or errors in the surface topography directly translate to the bed. In order to focus only on the broader features of the topography under the ice, the resulting bed profile is smoothed using a first-order Butterworth filter, which maintains locations of major features and the general shape of the bed but filters out higher-frequency roughness. The averaging length-scale of this filter is comparable to the typical longitudinal-coupling scale of 4–5 ice thicknesses for valley glaciers [*Echelmeyer and Kamb*, 1986; *Kamb and Echelmeyer*, 1986]. In the resulting bed profile (Figure 2b), the ice thicknesses are comparable to those of similar glaciers in Alaska, such as those derived from airborne ice-penetrating radar on the adjacent Bering glacier [*Conway et al.*, 2009] and bathymetric measurements in the bay formerly covered by Columbia Glacier [*O'Neel et al.*, 2005].

Table 1. Constants Used Within the Full Stress Glacier Flow Model[a]

Parameter	Symbol	Value
Density of ice [kg m^{-3}]	ρ_i	917
Flow rate factor [Pa^{-n} yr^{-1}]	A	6.8×10^{24}
Glen's Flow Law exponent	n	3
Sliding factor [m $Pa^{-(m-1)}$ yr^{-1}]	A_{sl}	tuning parameter
Sliding exponent	m	3

[a]Appendix A.

3.2. Evaluation and Improvement of the Thickness Estimate

[19] To refine the ice thickness estimate, as well as to define the basal properties relevant for erosion, a full-stress flowband model has been developed using the commercial, finite element software package COMSOL Multiphysics®. The basic model uses the plane strain momentum equations for nonlinear, temperate ice, based on the work of *Johnson and Staiger* [2007] and *Campbell* [2009]. While concerns have been raised about the model of *Johnson and Staiger* [2007], specifically of how their model generates velocities that are low over steep, shallow reaches [*Kavanaugh et al.*, 2009; *Golledge and Levy*, 2011], the incorporation of width variations following *Pattyn* [2002] and sliding (equation (A12)) within our model directly addresses many of these issues. The model is described in detail in Appendix A and parameters are given in Table 1.

[20] Using the initial thickness profile described in Section 3.1, we first compare the surface velocity distribution observed to that from the full-stress flowband model (Figures 3a and 3b). For the two ends of the study domain (from 0 to 5 km and from 34 to 40 km) the modeled velocities compare favorably with the observations. Toward the downstream end of the study domain, the match is to be expected because the known ice thickness in that location is used to set the value of A_{sl}, the constant in the sliding expression described in Appendix A. However, the surface velocities in the central portion of the domain are far too high, by up to a factor of 4. Equation (1) evidently overestimates the thickness in this region, presumably because it neglects the effects of both lateral shear and longitudinal stresses and oversimplifies the relationships between thickness, depth-averaged velocity and surface velocity.

[21] We now seek a simple bed profile for which the modeled velocity both matches the observed surface velocity in the flowband and is broadly consistent with a second constraint that the ice flux be approximately constant through this reach of the glacier. To generate these profiles, the central portion of the bed profile (between 5 km and 34 km; the edges are not modified from the initial bed found from mass conservation equation (1)) is modified by changing the elevations of three control points at 11 km, 23 km, and 27 km (two valleys and one ridge in Figure 4a), with a cubic-spline interpolation for points in between, until a better match to the observations is obtained. These points were chosen to correspond to distinctive regions of either very steep or very shallow ice surface slope. Based on sensitivity studies, similar to those described in Section 3.4, the ice thickness at each of these locations has a larger effect on surrounding flow than does the ice thickness at regions that have less extreme surface slopes. This smoothing of the bed

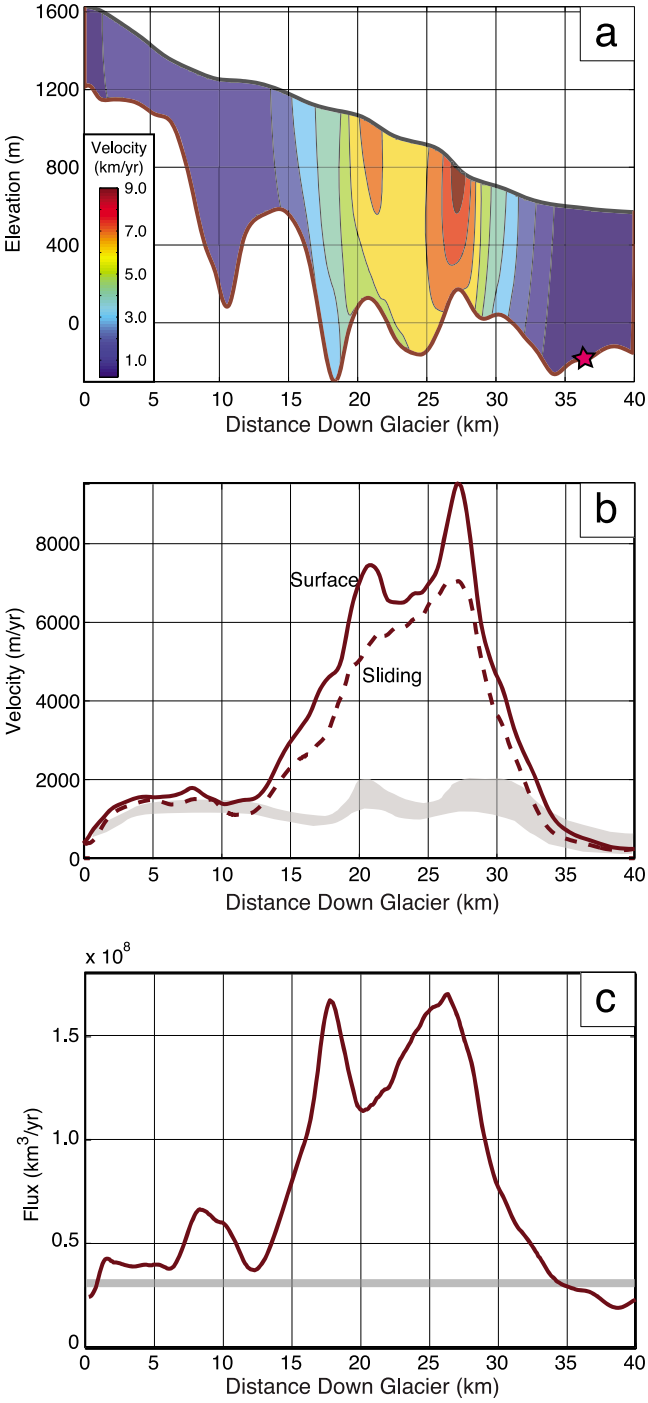

Figure 3. (a) Initial profiles of ice thickness and velocity along the length of Seward Throat with bed altitude based on equation (1), and the estimated ice flux at 37 km (red star) where the thickness has been measured; vertical exaggeration is x14. (b) Modeled surface velocity (solid line) and sliding (dashed line) velocity are much higher than the observed surface velocities (gray band). (c) Corresponding modeled ice flux through the flowband is also a poor fit compared to the known, uniform flux (gray band).

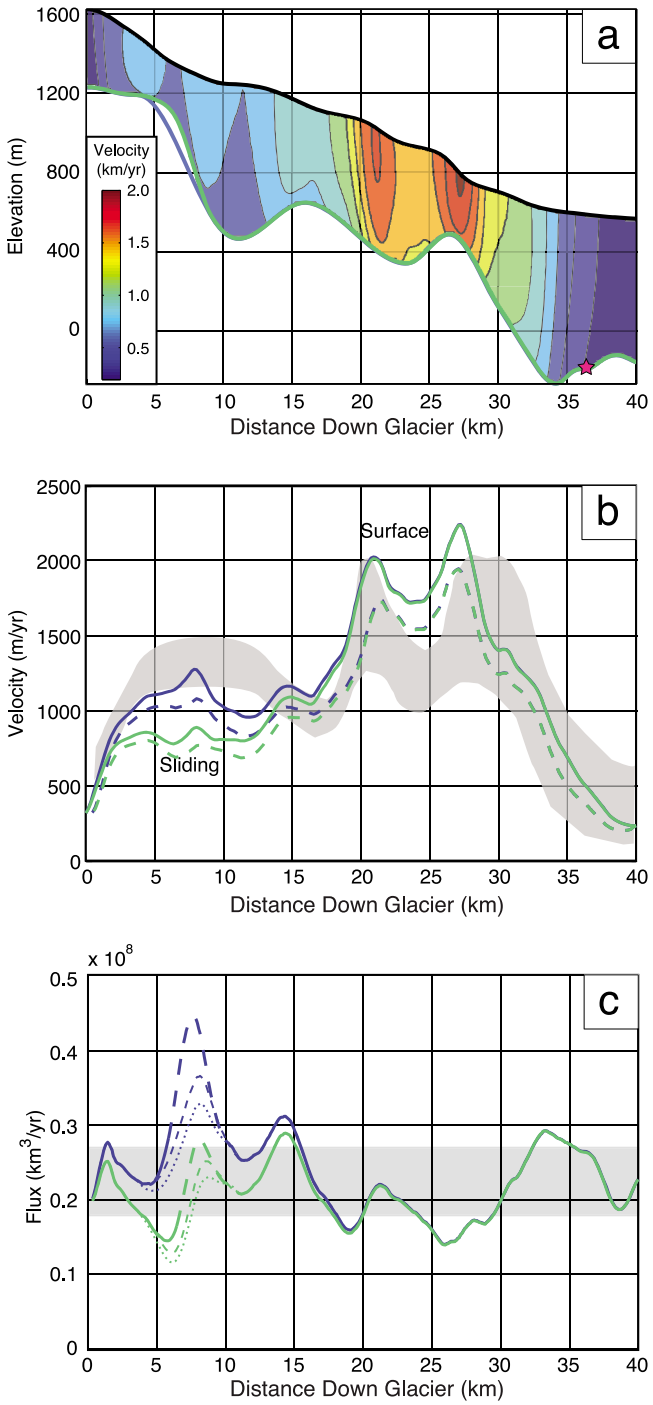

Figure 4. Longitudinal profiles of glacier surface and bed, inferred using the finite element model. Colored contours show horizontal velocities. (a) Two beds, the green line and the blue-dotted line, provide the best fits to either the flux and observed velocity field, respectively. (b) Modeled surface (solid lines) and sliding (dashed lines) velocities, corresponding to each bed, closely resemble the observed surface velocities (gray band). (c) Ice flux for each corresponding bed is relatively uniform, generally varying within 20% of the mean, a range shown in gray. The short-dashed and dotted flux profiles correspond to width profiles shown in the same way in Figure 2c.

enables us to focus on 5–10 km length-scale fluctuations and not on smaller scales. Figure 4a shows the geometry of two beds for which the full-stress model results are in reasonable accord with the constraints. Both of these beds differ significantly from the initial bed (Figure 3a); notably, the thickness is reduced by around 60% through the central portion of this reach. That such a large reduction in average thickness is required highlights the limitations of the initial scheme, in which we assume that the depth-averaged velocity and surface velocity were directly proportional. The full-stress model, which explicitly accounts for the effects of both shear and longitudinal stresses on the ice dynamics, highlights the sensitivity of velocity to ice thickness.

[22] Modeled results from the best fit beds should fall within the uncertainties in the observations and produce a reasonably constant ice flux; in order to not over-fit the observations, with their various uncertainties, we define a 20% window around the mean flux, which we expect to be reasonably constant through the Seward Throat (Figures 4b and 4c). The bed shown by the blue line produces the closest match to the observed surface velocities (Figure 4b), but it also produces an unrealistic peak in the ice flux near 7.5 km (Figure 4c). This peak is reduced by thinning the glacier in this region (Figure 4a), though there is a trade-off where this adjustment results in poorer agreement with the surface velocity (Figure 4b) and the uniform flux around 6 km. However, this is the region where the flowband is poorly defined (Figure 2), particularly the width. The three dashed line patterns between 3 km and 11 km for each bed profile (Figure 4c) were generated with the three-flowband width options in Figure 2c. Generally, by defining the width in a smoother manner, the agreement of the flux to a constant flux is improved. The other, smaller fluctuations in the flux can be accounted for by a variety of factors, as follows. Without knowledge of transient distortions to the glacier surface or a perfect model accounting for complexities of the setting (including lateral boundaries, non-uniform subglacial and englacial hydrology, bed roughness, etc.), there is no guarantee that all constraints can be met simultaneously. Further attempt to do so could risk over-fitting the data, require inserting spatial variations in processes without support of empirical data, or involve developing a formal inverse model. Therefore, we choose to not try to match the observations any more closely than shown in Figure 4. For these two best fit beds, the basic spatial pattern of ice velocity is robust, and similar to the observations, peaks between 20 and 30 km down the length of the glacier, with local maxima where surface slopes are steepest.

3.3. Improvements Over Previous Models

[23] Recent work with higher-order glacier dynamic models has shown that longitudinal stresses can strongly affect basal stresses [*Egholm et al.*, 2012]. We compare the current model, which directly computes all stresses, to the longitudinal-averaging method of *Kamb and Echelmeyer* [1986]. The Kamb and Echelmeyer method accounts for longitudinal stresses by smoothing the shear stresses found from the shallow ice approximation. A model using this scheme, while computationally simpler, would prove more difficult in determining reasonable values for the thickness by adding to the analysis another unknown, the smoothing scale, which itself depends on the main unknown, the

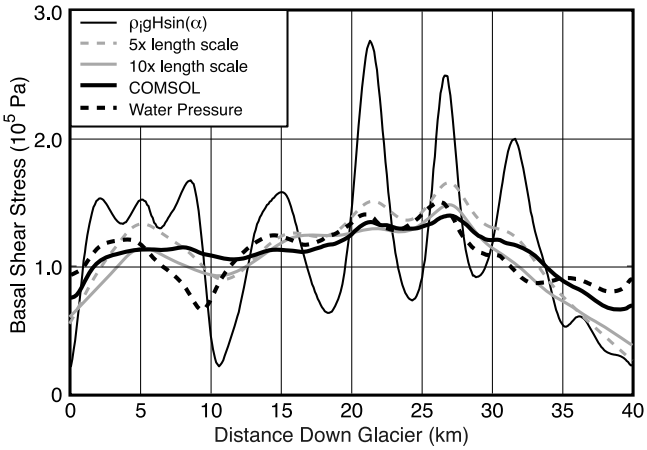

Figure 5. Heavy black solid and dashed lines show the basal shear stress as modeled in COMSOL Multiphysics® for the best fit bed, respectively without accounting for water pressure effects (solid blue line in Figure 4b), and with these effects (solid gray line in Figure 7). These basal stresses are compared to those from the shallow ice approximation (thin black line), and those using this approximation smoothed over 5 and 10 glacier thicknesses.

thickness. However, the full-stress model can provide a means for evaluating this smoothing scale for a given glacial geometry, which can be compared to the expected scales for glaciers [*Kamb and Echelmeyer*, 1986]. We find that in this case, when applying a smoothing length of 4 or 5 ice thicknesses (the commonly assumed values for valley glaciers), the resulting basal shear stress pattern fluctuates by more than 20% around that calculated directly from the numerical model (Figure 5). Even using 10 thicknesses for the smoothing scale produces more spatial variability in the basal shear stress than does the full-stress model. For the Seward Throat, the smoothing scale would need to exceed 10 ice thicknesses, which is more similar to that of ice streams [*Kamb and Echelmeyer*, 1986] (Figure 5). For these reasons, plus the relative ease with which COMSOL Multiphysics® can be used, we calculated the full-stress solution directly.

3.4. Sensitivity to Geometry and Basal Hydrology

[24] We now address the sensitivity of the modeled velocity and flux to the ice thickness and variations in the subglacial water pressure. Figure 6 shows the changes in surface velocity and flux resulting from changes to the bed profiles in sensitive regions, generally where the glacier surface is steep. The sensitivity to even small changes is high: elevating or depressing major transverse ridges by just 50 m, where the ice is around 500 m thick, changes the velocity by over 30% and the flux by over 50%. Similarly, moving the ridges horizontally by 1 km impacts the surface velocity by over 50% and the flux by almost 80%. This large sensitivity increases our confidence in our ice thickness profile, especially in key regions of rapid ice motion. Since these profiles yield surface-velocity and ice-flux patterns that generally fit our criteria to within 20%, we are capturing the ice-thickness profile at the kilometer scale.

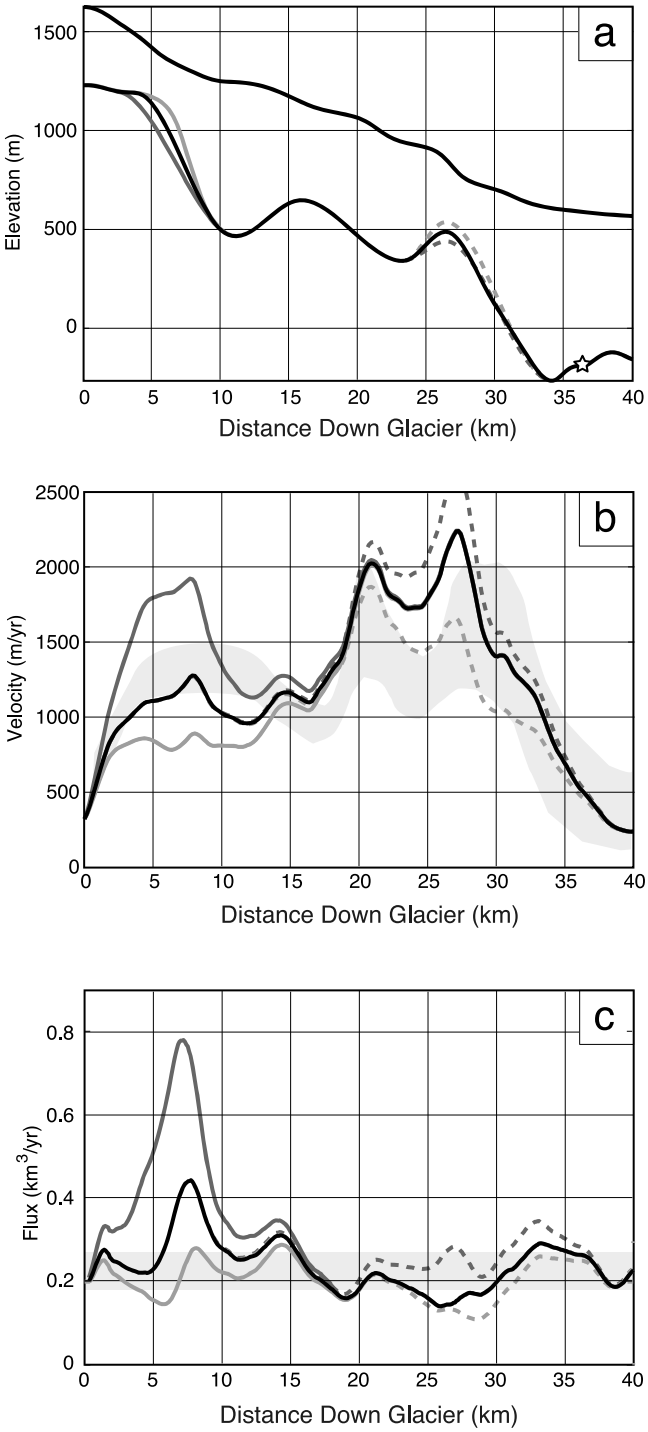

Figure 6. (a) Horizontal (solid gray lines) and vertical (dashed gray lines) bed adjustments for sensitivity analysis; ice surface and reference bed (black lines). (b) The resulting surface velocities (with respective line styles) from each profile are compared to the observed surface velocity distribution (gray band). (c) The resulting depth-averaged fluxes are compared with a 20% envelope around the initial flux (gray band). Horizontal shifts under shallow ice generally lead to steeper or shallower beds downstream, strongly affecting the surface velocity.

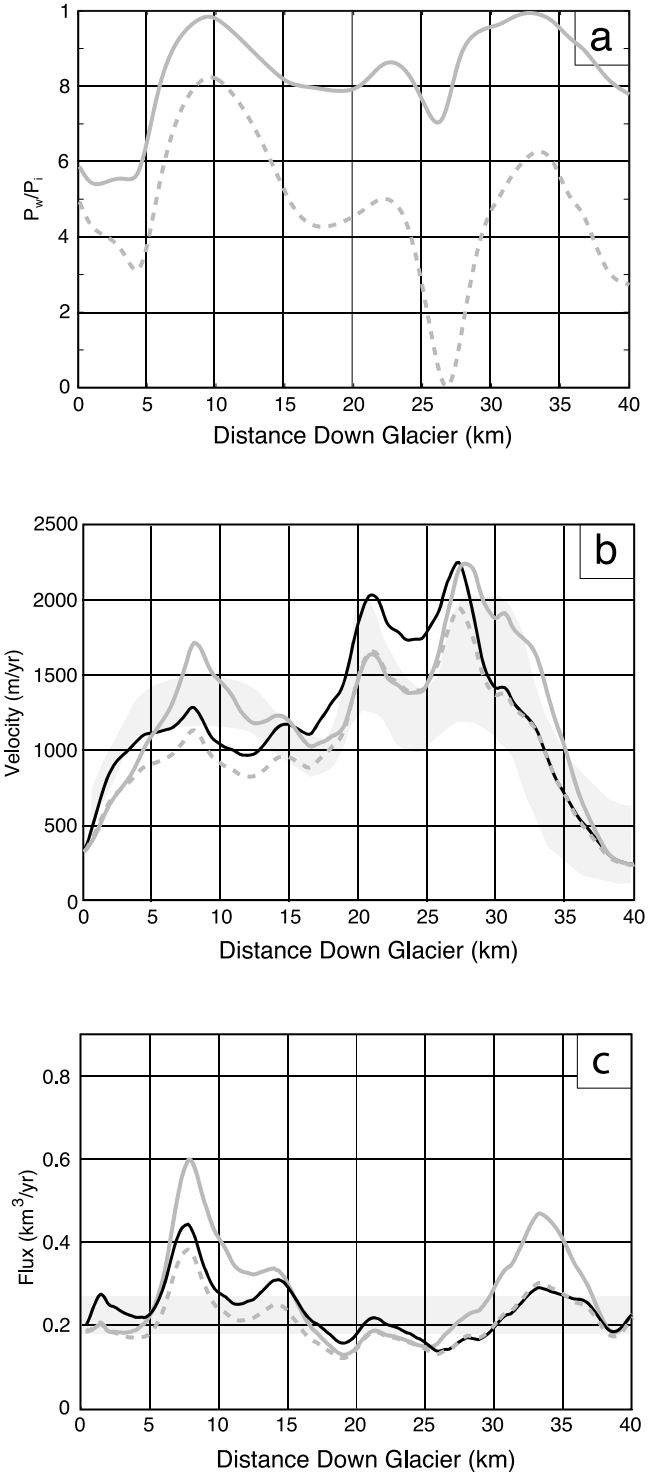

Figure 7. (a) The ratio of p_w to the overburden ice pressure p_i for two end-member hydraulic gradients (gray solid and dashed lines). (b) The resulting surface velocities (with respective line styles) from each profile are compared to the observed surface velocity distribution (gray band). (c) The resulting depth-averaged fluxes are compared with a 20% envelope around the initial flux (gray band). The modeled sliding velocity is sensitive to effective pressure, especially when it is very low (<20% of the overburden pressure).

[25] We now explore potential effects of the basal hydrology, simply abstracted, on the dynamics of this glacier through the study reach. Subglacial water is driven by the hydraulic potential gradient $\nabla\phi$ (e.g., Shreve, 1972): $\nabla\ \phi = \nabla\ p_w + \rho_w g\ \nabla\ z_b$, where z_b is the bed elevation and ρ_w is the density of water. Velocity distributions from two different water-pressure patterns are compared to the best fit profile shown in blue in Figure 4. For each of these water-pressure distributions, a constant hydraulic gradient is chosen to ensure that any water entering the Seward Throat must exit. Two gradients, both of which separately meet this criterion, are chosen in order to explore the sliding response to a range of corresponding water pressures, from p_w close to 0 to p_w close to ice pressure p_i (Figures 7a and 7b). The ratio of p_w to p_i can be used to visualize this response (Figure 7a), because it emphasizes these end-member cases. Where the water pressure approaches the ice pressure ($p_i = p_w$), the glacier nears flotation, and the sliding velocity increases dramatically.

[26] To focus on the pattern of velocity instead of its absolute magnitude, the value of A_{sl} in equation (A12) is rescaled for each calculation, so that the modeled surface velocity matches the observed surface velocity averaged over the reach. High water pressures induce large peaks in velocity (Figures 7a–7c), particularly around 8–9 km. Although this treatment of basal hydrology is very simple and neglects spatial variations in hydrologic impedance in the conduits, in the forms of sub-glacial and englacial drainages, and in water flux, it is still instructive. First, temporal variations in the subglacial water table, on the scale of those presented, could readily account for the seasonal and interannual variability in observed surface velocities (represented by the gray band in Figure 7c). Second, while more complex hydrology might affect the absolute magnitude of the velocity, the general pattern and the positions of the maxima and minima in surface velocities are not significantly impacted between different patterns of basal hydrology, likely due to the strong controls of the geometry.

4. Erosion Patterns

[27] The full-stress numerical flow line model of the glacier guided by surface data now enables us to quantitatively assess glacier variables that are likely to control erosion rates. We use these estimates to determine the spatial variation of glacial erosion with more confidence than models that use only the shallow ice approximation and lack constraints derived from glaciological measurements.

[28] Several equations have been proposed to represent glacial erosion rate; we use three of them. Most commonly, erosion rate $\dot{E}$ is proportional to some power of the sliding velocity u_{sl} [e.g., *Harbor et al.*, 1988; *Humphrey and Raymond*, 1994]:

$$\dot{E} = K|u_{sl}|^l, \tag{2}$$

where K is an erodibility factor dependent upon bedrock properties and basal conditions, and l is the exponent. Sparse empirical sediment-yield data from a glacier undergoing large changes in velocity suggest that this exponent is close to unity [*Humphrey and Raymond*, 1994]. Theoretical studies of the abrasion process suggest that the abrasion rate

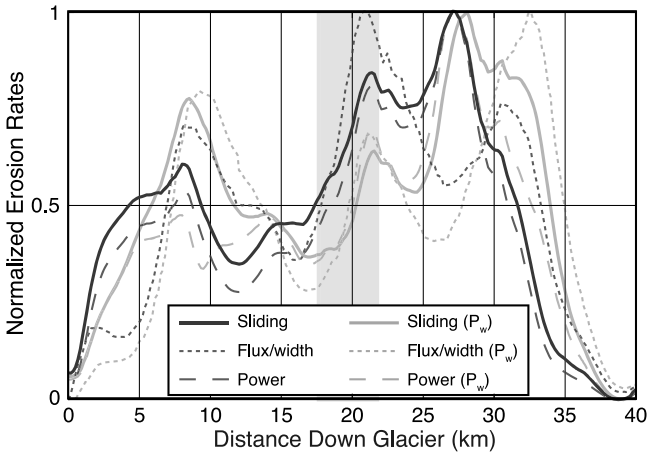

Figure 8. The longitudinal distribution of erosion rate, normalized to its maximum value, based on the sliding velocities from the best fit bed without water pressure effects (dark gray lines corresponding to green line in Figure 4) and with water pressure effects (light gray lines as in Figure 7). Results from assuming different dominant controls on erosion: sliding velocity (equation (2); solid lines), flux per unit width (equation (3); short-dashed lines), and basal power (equation (4); long-dashed lines). The gray vertical band shows broadly the location of the modern ELA [*Meier et al.*, 1972; *Péwé*, 1975]; it is notable that the regions of fastest erosion for all dominant controls on erosion barely overlap the ELA band.

scales with the sliding velocity squared [*Hallet*, 1979, 1981]. Because using larger exponents would not change the locations of maximum and minimum erosion, we investigate only $l = 1$ and focus our attention on the overall pattern of erosion, which is identical to the pattern of basal shear stress.

[29] Another form of the erosion rule holds that erosion rate scales with ice discharge (i.e., flux) per unit width, which is the depth-averaged velocity $\bar{u}$ multiplied by the ice thickness [e.g., *Kessler et al.*, 2008]:

$$\dot{E} = K_f \bar{u} H, \tag{3}$$

where K_f is an erodibility factor with units m^{-1} and plays a similar role as K in equation (2). Although the depth-averaged velocity does not scale directly with the sliding velocity, the advantage of this formulation is that climatic variables determining mass balance and associated balance flux can be easily linked to erosion.

[30] The rate at which energy is used in moving rocks in frictional contact with the bed determines abrasion rates [*Hallet*, 1979]. Generalizing to other erosion processes, the rate of energy dissipation, the power, at the glacier bed is likely to control glacial erosion rates. This glacier power has been used to compute erosion rates in large-scale ice sheet models [e.g., *Pollard and DeConto*, 2007]. It scales with the product of the sliding velocity and basal shear stress (τ_b), which has the advantage of taking into account the strength of the coupling between the ice and the bed, as well as the sliding velocity. For example, in cases where the ice approaches flotation, sliding tends to be fast, while erosion can be slow or vanishing because the ice-bed coupling is weak or non-existent. The erosion-power relationship can be expressed using another erodibility constant, K_p (Pa^{-1}):

$$\dot{E} = K_p u_{sl} \tau_b. \tag{4}$$

Figure 8 compares the spatial distribution of erosion rates based on these different erosion laws for the best fit bed both with and without the influence of water pressure-gradients (Figures 4a, 7a, and 7b, respectively). The profiles are normalized to their respective maximum erosion rate. The overall erosion-rate pattern is similar with all three erosion laws, because all the erosion laws depend on combinations of the velocity and basal shear stress. Highest erosion rates occur in the reach extending from 20 to 35 km, with a secondary maximum between 5 and 10 km.

[31] Relative to the Seward Ice Field and the Malaspina lobe, which both have significantly lower surface velocities, erosion is expected to be rapid over much of the Seward Throat (between 5 and 35 km), with two prominent peaks within the central portion (Figure 8). Glacier width can be a strong control on patterns of erosion rates [e.g., *Anderson et al.*, 2006], and this effect is evident where large volumes of ice are funneled through this narrow breach in the high ranges east of Mt. St. Elias. As climate and glacier lengths fluctuate over time, the Seward Throat would likely remain the locus of rapid erosion because of this funneling effect, sustaining rapid erosion influenced by the steep surface gradients and fast sliding.

[32] Finally, the numerical results show that the location of regions of rapid glacial erosion may be quite unrelated to the equilibrium line altitude (ELA). Lacking detailed glaciological information, it is commonly assumed that glacial erosion peaks at or near the ELA because the ice flux is largest there [e.g., *Andrews*, 1972; *Brozovic et al.*, 1997; *Berger et al.*, 2008]. While the regional, modern ELA (within the range of 1000–1100 m) [*Meier et al.*, 1972; *Péwé*, 1975] coincides generally with regions of fast erosion (from about 17 to 22 km in Figure 8), this was not the case throughout much of the Quaternary. For example, *Péwé* [1975] estimated that during the Last Glacial Maximum, the ELA was around 300 to 600 m lower than today. During this and comparable glaciations, glaciers were much thicker and longer, reaching the edge of the continental shelf, over 100 km south of the modern coastline [*Mann and Hamilton*, 1995; *Kaufman and Manley*, 2004; *Reece et al.*, 2011; Manley and Kaufman, online data, 2002]. Due to the shallow surface gradients and the substantial thickness of these glaciers, vertical changes in the ELA of hundreds of meters correspond to horizontal shifts in the equilibrium line along the ice surface of order of 100 km, as seen in numerical models of ice sheet fluctuations (for example, *Hooke and Fastook* [2007, Figure 4]). Specifically, the intersection of the Quaternary-average ELA with the ice surface likely occurred tens of kilometers south of the current shoreline. Therefore, we see no causative relation between the position of the modern ELA and the rapid exhumation in this region as suggested by *Berger et al.* [2008]. Moreover, in this region, that relation has also been questioned based on a reevaluation of thermochronometry data [*Enkelmann et al.*, 2010]. Rather, we suggest that the modern ELA and rapid erosion both reflect the rapid, localized uplift and the current climate and thus occur in the same area. The modern ELA and

freezing level generally parallel the mountains only a few tens of kilometers north of the coastline, since the mean annual temperature at sea level (+4°C) in this region is close to freezing. As the St. Elias Mountains rise sharply from the coastline, reflecting the interactions of the localized uplift and erosion, this is also exactly where there is sufficient relief to focus ice flow from large accumulation areas into narrow breaches through the mountains.

5. Implications for the Local Tectonic Setting

[33] The extensive geological and geophysical data sets available for the study area can be used to explore the relationship between the overall patterns of ongoing convergence and glacial erosion. Currently, based on GPS measurements of crustal motion, most of the 37 mm yr^{-1} plate convergence between the Yakutat block and southern Alaska is accommodated in a 70 km-wide zone south of the Seward Ice Field [*Elliott et al.*, 2010; *Elliott*, 2011]. This crustal deformation is localized on the multiple active faults that cut through the Seward Throat (Figure 1). Contemporary basin-wide erosion rates likely average between 5 and 10 mm yr^{-1} for the Seward-Malaspina glacier system [*Jaeger et al.*, 1998; *Sheaf et al.*, 2003]. As these rates average over the entire glacier basin, considerably higher rates through the Seward Throat are expected, possibly reaching 20 mm yr^{-1} or more, due to the exceptionally rapid, energetic sliding in this region (Figure 8). While modern erosion rates are not necessarily representative of rates on longer time scales, the relatively steady rates of offshore sedimentation over the Holocene suggest that the Seward-Malaspina glacier system and other glaciers in this coastal region have sustained erosion rates comparable to modern rates for at least 10000 years [*Jaeger et al.*, 1998; *Sheaf et al.*, 2003].

[34] Within the Seward Throat, it is difficult to relate specific structures to the subglacial topography and spatial pattern of erosion rates, because the location of structures is poorly known; the region is difficult to access and exposures are extremely limited due to the extensive cover of thick ice and snow. However, a striking feature of the reconstructed bed profiles (Figure 4a) is the presence of relatively narrow 50 to 100 m-high transverse ridges (for example at 15 km and 27 km). They are a robust feature in our analyses of ice thickness and are necessary for the flow model to match the observed surface velocities. We provide three hypotheses for why these ridges exist despite the extreme local erosion rates expected there (Figure 8). First, the ridges may be ephemeral, and we are just seeing a snapshot of the rapidly evolving topography, perhaps initiated by a recent pulse of local uplift due to folding or faulting. If this were the case, erosion rates approaching 20 mm yr^{-1} would eliminate a 100 m high ridge in just over 5000 years, which is an instant on the time scales of the orogen (>5 Ma). Second, the bedrock comprising the ridges may resist erosion more effectively than the bedrock in adjacent domains (i.e., via variations in K in (2)). Within the Seward Throat region, however, rock types do not vary considerably; generally, they are composed of the sedimentary cover of the Yakutat terrane, which is an unlikely candidate for erosion-resistant bedrock [*Plafker*, 1987; *Plafker et al.*, 1994]. The erodibility would have to vary by over an order of magnitude to render the erosion rates relatively uniform; otherwise the subglacial ridges under sustained erosion would still be ephemeral features. Third, the ridges might be sustained by localized uplift that keeps pace with the rapid localized erosion of the ridges. While a transverse ridge approaching steady state in this zone of rapid crustal convergence and erosion is an appealing concept, sustained uplift rates substantially exceeding 10 mm yr^{-1} seem unlikely. Corresponding exhumation rates on this scale have not been seen in thermochronology studies, though sampling has been sparse and could easily miss localized regions of rapid exhumation. Further geologic or geodetic study of the regions adjacent to the Seward Throat is needed to reveal which of these hypotheses, or which combination of them, best describes the nature of the topography below the glacier.

[35] Over the width of the full orogeny, which extends from the coast to the high mountains, there are significant variations in the lithologies and exhumational histories of the different terranes. Therefore, the erodibility (K in equation (3)) of the bedrock is also likely to vary significantly. *Enkelmann et al.* [2010] concluded that there must be a broad region of rapid uplift and exhumation below the ice of the Seward accumulation area, north of the Contact Fault, while *Spotila and Berger* [2010] postulated a more localized uplifting sliver (a few kilometers wide) in this region, with average erosion rates between 5 and 10 mm yr^{-1}. Relatively rapid erosion could occur in a region of slower and less energetic sliding, provided that the bedrock is particularly vulnerable to erosion (influencing K in equation (3)), perhaps because it is extensively strained and pervasively fractured [e.g., *Molnar et al.*, 2007]. This may well be the case for this region because it is centered on the transition from strike-slip to convergence at the NE corner of the Yakutat plate [e.g., *Meigs and Sauber*, 2000; *Enkelmann et al.*, 2008; *Koons et al.*, 2010].

[36] Based on existing observations, the general pattern of rapid erosion localized through the more mountainous region surrounding the Seward Throat is still expected based on geological and geophysical work. While the modern erosion rates likely exceed the Quaternary average [*Koppes and Montgomery*, 2009], reported exhumation rates in the orogen peak in the area surrounding the Seward Throat, ranging from 2 to 5 mm yr^{-1} over much of the orogen's development [*Berger and Spotila*, 2008]. For the major, highly erosive glaciers in the region, including the Seward-Malaspina System, the Icy Bay glaciers and Bering Glacier to the west, and glaciers terminating near Yakutat Bay to the east, erosion must generally match the uplift of the surrounding terrain to sustain both the topography and the glaciers. If erosion significantly outpaced rock uplift in the long-term, the high topography of the St. Elias Mountains would not persist, and the marine record would not show the distinct signal of continuous glaciation since 5.6 Ma [*Plafker*, 1987; *Lagoe et al.*, 1993; *Plafker et al.*, 1994; *Reece et al.*, 2011]. On the other hand, the Seward Throat could not persist as a major ice passage if erosion did not keep up with uplift. The rising mountains south of the Seward Ice Field would quickly block ice flow through the Seward Throat; for example, if we simply assume they rise 5 mm yr^{-1} and that erosion is negligible, they would form a km-high barrier in just 200,000 years.

[37] The localization of erosion and uplift has been shown to arise spontaneously in a large-scale, geodynamic model of coastal Alaska. Using a simple erosion rule where mass is

removed to maintain a constant elevation, *Koons et al.* [2010] found a large zone of localized uplift (and erosion) in a distinct region corresponding to the St. Elias Mountains. These results, along with the record of continuous and steady offshore sedimentation [*Jaeger et al.*, 1998] reinforce the idea of the Seward Throat as a region of localized and sustained erosion that is necessary for the maintenance of both the topography and offshore sedimentation.

6. Summary

[38] Observations of surface velocity, surface elevation and slope for the Seward-Malaspina glacier system are used with a full-stress glacier flow model both to estimate glacier thickness and to infer the spatial variability of glacial erosion rates in a tectonically active setting. As glacier thickness is difficult to measure under temperate ice, a robust method for determining the thickness is important, not only for understanding the basal processes but also for determining the subglacial topography and ice volumes that can help quantify the contribution of alpine glaciers to sea level rise [e.g., *Ackerly*, 1989; *Farinotti et al.*, 2009; *Fischer*, 2009; *Scherler et al.*, 2010]. For the Seward Throat, a simple mass conservation scheme for determining the ice thickness proves inadequate when the observed ice-surface velocities are compared to those derived from the higher-order model. Using the full-stress model and manual adjustments on the bed profile, we are able to define the glacier bed profile over length scales of several ice thickness, with observed velocity and flux constraints satisfied to within about 20%. The sensitivity of the model to a simple idealization of subglacial hydrology shows that the observed temporal variations can easily be accounted for by changes in subglacial water pressure, although complex subglacial conditions (such as transient hydrology or spatial heterogeneity in bed roughness) are beyond the scope of this analysis. On the other hand, the sensitivity of the model to slight changes to the bed topography underscores the robustness of our reconstructed bed profile.

[39] Using modeled glaciological variables relevant to erosion (basal shear stress, sliding velocity, and subglacial ice and water pressure), we examine the contemporary spatial variation of the glacial erosion rate along the length of the glacier. This is then interpreted within the geologic and geodynamic setting. Calculated erosion is fastest within the narrowest portion of the Seward Throat as basin geometry and valley width are the dominant controls on the erosion rates; the location of the ELA, which has significantly varied over the Quaternary, has little relevance. The overall pattern of ongoing crustal convergence and uplift, based on geodynamic modeling and geological and geophysical observations, is consistent with the broad region of relatively rapid erosion identified here. Our results may help guide more localized structural and geodetic research; steep and fast reaches of glaciers could serve as useful indicators of zones of active or recent uplift in regions where ice masses conceal the bedrock. The combination of detailed glacier measurements with a model well suited for complex glacier geometry and highly variable longitudinal stresses (and strain rates) is a powerful tool for realistically inferring the spatial variation of erosion rates and for assessing broader geodynamic and tectonic concepts often used in interpreting glaciated orogens.

Appendix A: Full-Stress, Flow Line Model Setup

A1. Glacier Flow Physics

[40] The glacier model solves equations for conservation of mass, momentum, and energy for prescribed material properties of ice and boundary conditions. For temperate glaciers, the temperature is at the pressure-melting point throughout, making the temperature dependence of any properties negligible. With this simplification, the glacier dynamics can then be described completely by conservation of mass and momentum. The coordinates for the glacier are defined by the unit vectors $\hat{\imath}$ in the x direction along the length of the glacier, $\hat{\jmath}$ in the y direction, across the width of the glacier; and z in the $\hat{k}$ direction on the vertical dimension of the glacier. The velocity is defined as $\mathbf{u} = u\hat{i} + v\hat{j} + w\hat{k}$ where u, v, and w are the velocity magnitudes. Most of this analysis, however, will be restricted to the along-flow line dimension defined by the xz plane down the center of the glacier, where sidewall drag is minimized. Therefore, the gradient vector is defined $\nabla = \frac{\partial}{\partial x}\hat{i} + \frac{\partial}{\partial z}\hat{k}$.

A1.1. Field Equations

[41] The conservation equations for mass and momentum are written

$$\nabla \cdot \mathbf{u} = 0, \tag{A1}$$

and

$$\frac{d\mathbf{u}}{dt} = \nabla \cdot \sigma + \rho_i g. \tag{A2}$$

For ice, the acceleration term ($\frac{d\mathbf{u}}{dt}$ in equation (A2)) is assumed to be negligible, so that $\nabla \cdot \sigma = -\rho_i g$.

[42] The general constitutive equation for glacier ice is commonly defined by Glen's Law of ice flow [*Paterson*, 1994, p. 85]

$$\dot{\varepsilon} = A\sigma^n, \tag{A3}$$

where A and n are constants determined empirically for polycrystalline ice. A is generally a function of temperature, and n is generally equal to 3 [*Paterson*, 1994, p. 85]. However, in the context of only temperate ice, A can be treated as a constant: $A = 6.8 \times 10^{24}$ Pa^{-3} yr^{-1} [*Paterson*, 1994, p. 97].

[43] More generally, we can define the relationship between stress (σ'_{ij} is the deviatoric stress tensor) and strain rate, $\dot{\varepsilon}_{ij}$ as a viscous flow equation

$$\sigma'_{ij} = 2\eta\dot{\varepsilon}_{ij}, \tag{A4}$$

where the viscosity η can be defined in terms of Glen's Law (A4)

$$\eta = \frac{1}{2}A^{-\frac{1}{n}}\dot{\varepsilon}^{\frac{1-n}{n}}, \tag{A5}$$

and the second invariant of the strain rate is

$$\dot{\varepsilon}^2 = \frac{1}{2}\sum_{ij}\dot{\varepsilon}_{ij}\dot{\varepsilon}_{ij}. \tag{A6}$$

The strain rates are defined by the velocity gradients as such

$$\begin{pmatrix} \dot{\varepsilon}_{xx} & \dot{\varepsilon}_{xz} \\ \dot{\varepsilon}_{zx} & \dot{\varepsilon}_{zz} \end{pmatrix} = \begin{pmatrix} \frac{\partial u}{\partial x} & \frac{1}{2}\left(\frac{\partial u}{\partial z}+\frac{\partial w}{\partial x}\right) \\ \frac{1}{2}\left(\frac{\partial u}{\partial z}+\frac{\partial w}{\partial x}\right) & \frac{\partial w}{\partial z} \end{pmatrix}. \tag{A7}$$

Substituting equation (A7) into equation (A5) yields the dynamic viscosity as a function of only the velocity gradients and constants:

$$\eta = \frac{1}{2}A^{-\frac{1}{n}}\left(\left(\frac{\partial u}{\partial x}\right)^2 + \frac{1}{4}\left(\frac{\partial u}{\partial z}+\frac{\partial w}{\partial x}\right)^2\right)^{\frac{1-n}{2n}}. \tag{A8}$$

A1.2. Width Variations

[44] The model considered so far has been a 2D flow line where the flow neither diverges nor converges. In order to accurately model even a 2D cross section from a glacier with variable width, incorporating effects on the flux per unit width, and on the dynamic viscosity due to convergence and divergence are required.

[45] For a flowband with varying width, $W(x)$, the equations of mass conservation can be modified to incorporate the transverse divergence of flow (nonzero $\frac{\partial v}{\partial y}$). Following *Pattyn* [2002], transverse velocity gradients follow the width variations, such that $\frac{\partial v}{\partial y} = \frac{u}{W}\left(\frac{\partial W}{\partial x}\right)$. With this incorporated into the conservation of mass, equation (A1) is modified such that

$$\frac{\partial u}{\partial x} + \frac{u}{W}\left(\frac{\partial W}{\partial x}\right) + \frac{\partial w}{\partial z} = 0. \tag{A9}$$

In turn the dynamic viscosity is redefined to incorporate these changes.

$$\eta = \frac{1}{2}A^{-\frac{1}{n}}\left(\left(\frac{\partial u}{\partial x}\right)^2 + \left(\frac{u}{W}\left(\frac{\partial W}{\partial x}\right)\right)^2 + \frac{u}{W}\frac{\partial u}{\partial x}\frac{\partial W}{\partial x} + \frac{1}{4}\left(\frac{\partial u}{\partial z}+\frac{\partial w}{\partial x}\right)^2\right)^{\frac{1-n}{2n}}. \tag{A10}$$

A shape factor is also incorporated to account for the gravitational force that is partially supported by the valley walls [*Paterson*, 1994, pp. 267–270]. *Nye* [1965] and *Budd* [1969] found analytical solutions for the shape factor due to a variety of different valley cross-section shapes, including rectilinear, parabolic, and semi-circular. For our model, a parabolic valley profile is assumed, and the shear stress modifier, $F_s(x)$, can be found from the ratio of the valley width (W_v) to the ice thickness (H) at any point along the profile, using a simple lookup table based upon *Paterson* [1994, Table 11.3, p. 269]. This is directly applied to the shear stress such that $\tau_{xz} = 2F_s\eta\dot{\varepsilon}_{xz}$.

A1.3. Sliding, Calibration, and Other Boundary Conditions

[46] Boundary conditions are applied to the top and bottom surfaces of the glacier as well as perpendicular to the flow at the entrance and exit of the flow band. The upper surface of the glacier is stress free such that

$$\left[-p\mathbf{I} + \eta\left(\nabla\mathbf{u} + (\nabla\mathbf{u})^T\right)\right]\hat{n} = 0, \tag{A11}$$

where $\mathbf{I}$ is the identity matrix and $\hat{n}$ is a normal vector pointing out of the boundary. The bottom of the glacier can be sliding, at a speed that is given by the commonly accepted rule [*Budd et al.*, 1979; *Bindschadler*, 1983; *Anderson et al.*, 2004]:

$$u_{sl} = A_{sl}\frac{\tau_b^m}{p_i - p_w}, \tag{A12}$$

where m is a sliding exponent (Table 1), τ_b is the basal shear stress calculated in the model, and the denominator, which is commonly known as the effective pressure p_{eff}, is the difference between ice overburden pressure p_{i} and water pressure p_{w} [e.g., *Budd et al.*, 1979; *Bindschadler*, 1983; *Anderson et al.*, 2004]. Except for the sensitivity studies, discussed in Section 3.3, a simplified version of equation (A12) is used such that $u_{sl} = A_{sl}\tau_b^m$. A_{sl} is a sliding factor that is assumed constant over the length of the glacier. We determine A_{sl} by assuming that, at x = 36 km where the thickness was measured (Figure 2), the difference between the observed surface velocity and the modeled deformational velocity (u_{def}) evaluated at the surface is the sliding velocity, then A_{sl} is solved found from equation (A12) such that $A_{sl} = (u_{obs} - u_{def}(z_s))(p_i - p_w)\tau_b^{-m}$. Where water pressure is not considered, this becomes $A_{sl} = (u_{obs} - u_{def}(z_s))\tau_b^{-m}$. As u_{def} is influenced by the sliding velocity, the model was manually iterated using different values of A_{sl} until the total surface velocity matched the observed surface velocity at x = 36 km.

[47] For modeling a specific reach within a glacier, the vertical edges are set up so that an input velocity, $u_{in}(x_0,z)$, is given at the upstream boundary, and an output velocity, $u_{out}(x_L,z)$, is given at the downstream boundary, with the flow specified perpendicular to the boundaries. In general, the model has been found to be rather insensitive to the lateral boundary conditions, so the simplest assumption of plug flow is used, though depth-variable velocity profiles have also been tested. For regions farther than 5 km from these boundaries, the velocity distributions were not found to be influenced by these conditions. For the rest of the profile, the velocity at the lower boundary (sliding velocity) is calculated within the model. For the velocity profiles (Figures 3, 4, 6, and 7), the u_{in} and u_{out} are assumed to be 90% of the observed surface velocity: $u_{in}(x_0,z) = 0.9\ u_{surf}(x_0)$ and $u_{out}(x_L,z) = 0.9\ u_{surf}(x_L)$.

A2. COMSOL Multiphysics® Setup

[48] A commercial finite element package, COMSOL Multiphysics®, is used for modeling glacier flow by solving the momentum conservation equations for a given geometry

and boundary conditions to extend the work of *Johnson and Staiger* [2007] and *Campbell* [2009]. The finite element method (FEM) is well suited to the complex geometries of glaciers, because a regular mesh is not needed. COMSOL uses Lagrange quadratic elements for accurate computing of the second derivative of velocity [*Johnson and Staiger*, 2007]. Due to the viscosity (equation (A10)), this is a nonlinear system, which is solved within COMSOL using the modified Newton iterative solver [*Deuflhard*, 1974]. The resulting linear system is solved by the UMFPACK linear solver [*Davis*, 2004].

[49] Within the COMSOL environment, the built-in meshing algorithms were used. No scaling of the glacier physics is needed, which is a departure from other models [*Pattyn*, 2002]. The mesh is chosen to be a physics-generated (General Physics) mesh of "Normal" size. However, because the glacier thickness is significantly less than its width or span, the mesh is scaled to be finer in the vertical dimension than in the horizontal by a factor of 10. For the best fit bed profile (blue line in Figure 4), there are 5502 triangular elements, including 496 edge elements and 442 vertex elements.

[50] **Acknowledgments.** This material is based upon work supported by the National Science Foundation under grant 0409884 and EAR-0735402 within the St. Elias Erosion and Tectonics Project (STEEP). We gladly thank Howard Conway for providing data on the ice thickness, Evan Burgess for discussing the temporal variation of the velocity through the Seward Throat, Adam Campbell and Bruce Finlayson for invaluable help with the COMSOL Multiphysics® modeling environment, and Julie Elliot for discussions about the St. Elias geodetics. Finally, we thank Frederic Herman, Dylan Ward, Nicholas Golledge, and the JGR editor, Bryn Hubbard, for very helpful and in-depth reviews.

References

Ackerly, S. C. (1989), Reconstructions of mountain glacier profiles, northeastern United States, *Geol. Soc. Am. Bull.*, *101*(4), 561–572, doi:10.1130/0016-7606(1989)101<0561:ROMGPN>2.3.CO;2.

Allen, C. R., and G. I. Smith (1953), Seismic and gravity investigations on the Malaspina Glacier, Alaska, *Eos Trans. AGU*, *34*(5), 755–760.

Anderson, R. S., S. P. Anderson, K. R. MacGregor, E. D. Waddington, S. O'Neel, C. A. Riihimaki, and M. G. Loso (2004), Strong feedbacks between hydrology and sliding of a small alpine glacier, *J. Geophys. Res.*, *109*, F03005, doi:10.1029/2004JF000120.

Anderson, R. S., P. Molnar, and M. A. Kessler (2006), Features of glacial valley profiles simply explained, *J. Geophys. Res.*, *111*, F01004, doi:10.1029/2005JF000344.

Andrews, J. T. (1972), Glacier power, mass balances, velocities and erosion potential, *Z. Geomorphol.*, *13*, 1–17.

Arendt, A. A., S. B. Luthcke, C. F. Larsen, W. Abdalati, W. B. Krabill, and M. J. Beedle (2008), Validation of high-resolution GRACE mascon estimates of glacier mass changes in the St Elias Mountains, Alaska, USA, using aircraft laser altimetry, *J. Glaciol.*, *54*(188), 778–787, doi:10.3189/002214308787780067.

Beaumont, C., P. Fullsack, and J. Hamilton (1992), Erosional control of active compressional orogens, in *Thrust Tectonics*, edited by K. R. McClay, pp. 1–18, Chapman and Hall, New York, doi:10.1007/978-94-011-3066-0_1.

Berger, A. L., and J. A. Spotila (2008), Denudation and deformation in a glaciated orogenic wedge: The St. Elias orogen, Alaska, *Geology*, *36*(7), 523–526, doi:10.1130/G24883A.1.

Berger, A. L., et al. (2008), Quaternary tectonic response to intensified glacial erosion in an orogenic wedge, *Nat. Geosci.*, *1*(11), 793–799, doi:10.1038/ngeo334.

Bindschadler, R. (1983), The importance of pressurized subglacial water in separation and sliding at the glacier bed, *J. Glaciol.*, *29*(101), 3–19.

Bookhagen, B., R. C. Thiede, and M. R. Strecker (2005), Late Quaternary intensified monsoon phases control landscape evolution in the northwest Himalaya, *Geology*, *33*(2), 149–152, doi:10.1130/G20982.1.

Brozovic, N., D. W. Burbank, and A. J. Meigs (1997), Climatic limits on landscape development in the northwestern Himalaya, *Science*, *276*(5312), 571–574, doi:10.1126/science.276.5312.571.

Bruhn, R. L., T. L. Pavlis, G. Plafker, and L. Serpa (2004), Deformation during terrane accretion in the Saint Elias orogen, Alaska, *Geol. Soc. Am. Bull.*, *116*(7–8), 771–787, doi:10.1130/B25182.1.

Budd, W. F. (1969), The dynamics of ice masses, *Sci. Rep. 108*, Aust. Natl. Antarct. Res. Exped., Melbourne.

Budd, W. F., P. L. Keage, and N. A. Blundy (1979), Empirical studies of ice sliding, *J. Glaciol.*, *23*(89), 157–170.

Burgess, E., R. Forster, and D. Hall (2010), Regional Observations of Alaska Glacier Dynamics, Abstract C23A-0582 presented at 2010 Fall Meeting, AGU, San Francisco, Calif., 13–17 Dec.

Campbell, A. J. (2009), Numerical Model investigation of Crane Glacier response to collapse of the Larsen B ice shelf, Antarctic Peninsula, MS thesis, Dep. of Geol., Portland State Univ., Portland, Oreg.

Chapman, J. B., et al. (2008), Neotectonics of the Yakutat collision: Changes in deformation driven by mass redistribution, in *Active Tectonics and Seismic Potential of Alaska*, *Geophys. Monogr. Ser.*, vol. 179, edited by J. T. Freymueller et al., pp. 65–81, AGU, Washington, D.C., doi:10.1029/179GM04

Conway, H., B. Smith, P. Vaswani, K. Matsuoka, E. Rignot, and P. Claus (2009), A low-frequency ice-penetrating radar system adapted for use from an airplane: Test results from Bering and Malaspina Glaciers, Alaska, *Ann. Glaciol.*, *50*, 93–97, doi:10.3189/172756409789097487.

Davis, T. (2004), A column pre-ordering strategy for the unsymmetric- pattern multifrontal method, *AMS Trans. Math. Software*, *30*, 165–195.

Delmas, M., M. Calvet, and Y. Gunnet (2009), Variability of Quaternary glacial erosion rates: A global perspective with special reference to the Eastern Pyrenees, *Quat. Sci. Rev.*, *28*(5–6), 484–498, doi:10.1016/j.quascirev.2008.11.006.

Deuflhard, P. (1974), A modified Newton method for the solution of ill-conditioned systems of nonlinear equations with application to multiple shooting, *Numer. Math.*, *22*, 289–315.

Echelmeyer, K. A., and B. Kamb (1986), Stress-gradient coupling in glacier flow: II. Longitudinal averaging of the flow response to small perturbations in ice thickness and surface slope, *J. Glaciol.*, *32*, 285–298.

Egholm, D. L., V. K. Pedersen, M. F. Knudsen, and N. K. Larsen (2012), On the importance of higher order ice dynamics for glacial landscape evolution, *Geomorphology*, *141–142*, 67–80, doi:10.1016/j.geomorph.2011.12.020.

Elliott, J. (2011), Active tectonics in southern Alaska and the role of the Yakutat Block constrained by GPS measurements, PhD thesis, Geophys. Inst., Univ. of Alaska Fairbanks, Fairbanks.

Elliott, J. L., C. F. Larsen, J. T. Freymueller, and R. J. Motyka (2010), Tectonic block motion and glacial isostatic adjustment in southeast Alaska and adjacent Canada constrained by GPS measurements, *J. Geophys. Res.*, *115*, B09407, doi:10.1029/2009JB007139.

Enkelmann, E., J. I. Garver, and T. L. Pavlis (2008), Rapid exhumation of ice-covered rocks of the Chugach–St. Elias orogen, Southeast Alaska, *Geology*, *36*(12), 915–918, doi:10.1130/G2252A.1.

Enkelmann, E., P. K. Zeitler, J. I. Garver, T. L. Pavlis, and B. P. Hooks (2010), The thermochronological record of tectonic and surface process interaction at the Yakutat-North American collision zone in southeast Alaska, *Am. J. Sci.*, *310*(4), 231–260, doi:10.2475/04.2010.01.

Farinotti, D., M. Huss, A. Bauder, M. Funk, and M. Truffer (2009), A method to estimate the ice volume and ice-thickness distribution of alpine glaciers, *J. Glaciol.*, *55*(191), 422–430, doi:10.3189/002214309788816759.

Fischer, A. (2009), Calculation of glacier volume from sparse ice-thickness data, applied to Schaufelferner, Austria, *J. Glaciol.*, *55*(191), 453–460, doi:10.3189/002214309788816740.

Ford, A. L. J., R. R. Forster, and R. L. Bruhn (2003), Ice surface velocity patterns on Seward Glacier, Alaska-Yukon, and their implications for regional tectonics in the Saint Elias Mountains, *Ann. Glaciol.*, *36*, 21–28, doi:10.3189/172756403781816086.

Golledge, N. R., and R. H. Levy (2011), Geometry and dynamics of an East Antarctic Ice Sheet outlet glacier, under past and present climates, *J. Geophys. Res.*, *116*, F03025, doi:10.1029/2011JF002028.

Gordon, S., M. Sharp, B. Hubbard, C. Smart, B. Ketterling, and I. Willis (1998), Seasonal reorganization of subglacial drainage inferred from measurements in boreholes, *Hydrol. Processes*, *12*(1), 105–133, doi:10.1002/(SICI)1099-1085(199801)12:1<105::AID-HYP566>3.0.CO;2-#.

Hallet, B. (1979), A theoretical model of glacial abrasion, *J. Glaciol.*, *23*(89), 39–50.

Hallet, B. (1981), Glacial abrasion and sliding: their dependence on the debris concentration in basal ice, *Ann. Glaciol.*, *2*, 23–28.

Hallet, B. (1996), Glacial quarrying: A simple theoretical model, *Ann. Glaciol.*, *22*, 1–8.

Harbor, J. M., B. Hallet, and C. F. Raymond (1988), A numerical model of landform development by glacial erosion, *Nature*, *333*(6171), 347–349, doi:10.1038/333347a0.

Harper, J. T., N. F. Humphrey, W. T. Pfeffer, T. Fudge, and S. O'Neel (2005), Evolution of subglacial water pressure along a glacier's length, *Ann. Glaciol.*, *40*, 31–36, doi:10.3189/172756405781813573.

Headley, R., B. Hallet, and E. Rignot (2007), Measurements of fast ice flow of the Malaspina glacier to explore connections between glacial erosion and crustal deformation in the St. Elias Mountains, Alaska, *Eos Trans. AGU*, *88*(52), Fall Meet. Suppl., Abstract C41A-0050.

Herman, F., and J. Braun (2008), Evolution of the glacial landscape of the Southern Alps of New Zealand: Insights from a glacial erosion model, *J. Geophys. Res.*, *113*, F02009, doi:10.1029/2007JF000807.

Hooke, R. L. B., and J. Fastook (2007), Thermal conditions at the bed of the Laurentide ice sheet in Maine during deglaciation: Implications for esker formation, *J. Glaciol.*, *53*(183), 646–658, doi:10.3189/002214307784409243.

Humphrey, N. F., and C. F. Raymond (1994), Hydrology, erosion and sediment production in a surging glacier: Variegated Glacier, Alaska, 1982–83, *J. Glaciol.*, *40*(136), 539–552.

Jaeger, J. M., C. A. Nittrouer, N. D. Scott, and J. D. Milliman (1998), Sediment accumulation along a glacially impacted mountainous coastline: North-east Gulf of Alaska, *Basin Res.*, *10*(1), 155–173, doi:10.1046/j.1365-2117.1998.00059.x.

Johnson, J. V., and J. W. Staiger (2007), Modeling long-term stability of the Ferrar Glacier, East Antarctica: Implications for interpreting cosmogenic nuclide inheritance, *J. Geophys. Res.*, *112*, F03S30, doi:10.1029/2006JF000599.

Kamb, B., and K. A. Echelmeyer (1986), Stress-gradient coupling in glacier flow: I. Longitudinal averaging of the influence of ice thickness and surface slope, *J. Glaciol.*, *32*, 267–284.

Kaufman, D. S., and W. F. Manley (2004), Pleistocene maximum and Late Wisconsinan glacier extents across Alaska, USA, in *Quaternary Glaciations: Extent and Chronology, Part II: North America*, *Dev. in Quat. Sci.*, vol. 2, edited by J. Ehlers and P. L. Gibbard, pp. 427–445, Elsevier, Amsterdam.

Kavanaugh, J. L., K. M. Cuffey, D. L. Morse, H. Conway, and E. Rignot (2009), Dynamics and mass balance of Taylor Glacier, Antarctica: 1. Geometry and surface velocities, *J. Geophys. Res.*, *114*, F04010, doi:10.1029/2009JF001309.

Kessler, M. A., R. S. Anderson, and J. P. Briner (2008), Fjord insertion into continental margins driven by topographic steering of ice, *Nat. Geosci.*, *1*(6), 365–369, doi:10.1038/ngeo201.

Koons, P. O. (1995), Modeling the topographic evolution of collisional belts, *Annu. Rev. Earth Planet. Sci.*, *23*(1), 375–408, doi:10.1146/annurev.ea.23.050195.002111.

Koons, P. O., B. P. Hooks, T. Pavlis, P. Upton, and A. D. Barker (2010), Three-dimensional mechanics of Yakutat convergence in the southern Alaskan plate corner, *Tectonics*, *29*, TC4008, doi:10.1029/2009TC002463.

Koppes, M., and B. Hallet (2006), Erosion rates during rapid deglaciation in Icy Bay, Alaska, *J. Geophys. Res.*, *111*, F02023, doi:10.1029/2005JF000349.

Koppes, M. N., and D. R. Montgomery (2009), The relative efficacy of fluvial and glacial erosion over modern to orogenic timescales, *Nat. Geosci.*, *2*(9), 644–647, doi:10.1038/ngeo616.

Lagoe, M. B., C. H. Eyles, N. Eyles, and C. Hale (1993), Timing of late Cenozoic tidewater glaciation in the far North Pacific, *Geol. Soc. Am. Bull.*, *105*(12), 1542–1560, doi:10.1130/0016-7606(1993)105<1542:TOLCTG>2.3.CO;2.

Mann, D. H., and T. D. Hamilton (1995), Late Pleistocene and Holocene paleoenvironments of the North Pacific coast, *Quat. Sci. Rev.*, *14*(5), 449–471, doi:10.1016/0277-3791(95)00016-I.

Meier, M. F., and A. S. Post (1962), Recent variations in mass net budgets of glaciers in western North America, *Int. Assoc. Hydrol. Sci.*, *58*, 63–77.

Meier, M. F., W. V. Tangborn, and L. R. Mayo (1972), Combined ice and water balances of Gulkana and Wolverine glaciers, Alaska, and South Cascade glacier, Washington; 1965 and 1966 Hydrologic Years, *U.S. Geol. Surv. Prof. Pap.*, *715-A*, 23, doi:10.1017/S001675680003987X.

Meigs, A., and J. Sauber (2000), Southern Alaska as an example of the long-term consequences of mountain building under the influence of glaciers, *Quat. Sci. Rev.*, *19*(14–15), 1543–1562, doi:10.1016/S0277-3791(00)00077-9.

Meigs, A., S. Johnston, and J. Garver (2008), Crustal-scale structural architecture, shortening, and exhumation of an active, eroding orogenic wedge (Chugach/St Elias Range, southern Alaska), *Tectonics*, *27*, TC4003, doi:10.1029/2007TC002168.

Michel, R., and E. Rignot (1999), Flow of Glaciar Moreno, Argentina, from repeat-pass Shuttle Imaging Radar images: Comparison of the phase correlation method with radar interferometry, *J. Glaciol.*, *45*(149), 93–100.

Molnar, P., and P. England (1990), Late Cenozoic uplift of mountain ranges and global climate change: Chicken or egg?, *Nature*, *346*(6279), 29–34, doi:10.1038/346029a0.

Molnar, P., R. S. Anderson, and S. P. Anderson (2007), Tectonics, fracturing of rock, and erosion, *J. Geophys. Res.*, *112*, F03014, doi:10.1029/2005JF000433.

Molnia, B. F. (1986), Glacial history of the northeastern Gulf of Alaska; a synthesis, in *Glaciation in Alaska–The Geologic Record*, edited by T. D. Hamilton, K. M. Reed, and R. M. Thorson, pp. 219–235, Alaska Geol. Soc., Anchorage, AK.

Muskett, R. R., C. S. Lingle, J. M. Sauber, A. S. Post, W. V. Tangborn, and B. T. Rabus (2008), Surging, accelerating surface lowering and volume reduction of the Malaspina Glacier system, Alaska, USA, and Yukon, Canada, from 1972 to 2006, *J. Glaciol.*, *54*, 788–800, doi:10.3189/002214308787779915.

Nye, J. F. (1965), The flow of a glacier in a channel of rectangular, elliptic or parabolic cross-section, *J. Glaciol.*, *5*(41), 661–690.

O'Neel, S., W. T. Pfeffer, R. Krimmel, and M. Meier (2005), Evolving force balance at Columbia Glacier, Alaska, during its rapid retreat, *J. Geophys. Res.*, *110*, F03012, doi:10.1029/2005JF000292.

Paterson, W. S. B. (1994), Physics of Glaciers, 3rd ed., Butterworth-Heinemann, Burlington, Mass

Pattyn, F. (2002), Transient glacier response with a higher-order numerical ice-flow model, *J. Glaciol.*, *48*(162), 467–477, doi:10.3189/172756502781831278.

Pavlis, G. L., N. A. Ruppert, R. A. Hansen, and A. Panessal (2008), Seismicity of southeast Alaska: Links between fault geometry and glaciers, *Eos Trans. AGU*, *89*(53), Fall Meet. Suppl., Abstract T53B-1946.

Péwé, T. L. (1975), Quaternary geology of Alaska, *U.S. Geol. Surv. Prof. Pap.*, *835*, 139 pp.

Plafker, G. (1987), Regional geology and petroleum potential of the northern Gulf of Alaska continental margin, in *Geology and Resource Potential of the Continental Margin of Western North America and Adjacent Ocean Basins—Beaufort Sea to Baja California*, *Earth Sci. Ser.*, vol. 6, edited by D. W. Scholl, A. Grantz, and J. G. Vedder, pp. 229–268, Circum-Pac. Counc. for Energy and Min. Resour., Houston, Tex.

Plafker, G., J. C. Moore, and G. R. Winkler (1994), Geology of the southern Alaska margin, in *The Geology of Alaska*, *Geol. of North Am.*, vol. G-1, edited by G. Plafker and H. C. Berg, pp. 389–450, Geol. Soc. Am., Boulder, Colo.

Pollard, D., and R. M. R. M. DeConto (2007), A coupled ice-sheet/ice-shelf/sediment model applied to a marine-margin flow line: Forced and unforced variations, *Glacial Sediment. Processes Prod.*, *39*, 37–52, doi:10.1002/9781444304435.ch4.

Porter, S. C. (1989), Late Holocene fluctuations of the fiord glacier system in Icy Bay, Alaska, U.S.A, *Arct. Alp. Res.*, *21*(4), 364–379, doi:10.2307/1551646.

Rasmussen, A. L. (1989), Surface velocity variations of the lower part of the Columbia Glacier, Alaska, 1977–1981, *U.S. Geol. Surv. Prof. Pap.*, *1258-H*, 52 pp.

Reece, R. S., S. P. S. Gulick, B. K. Horton, G. L. Christeson, and L. L. Worthington (2011), Tectonic and climatic influence on the evolution of the Surveyor Fan and Channel system, Gulf of Alaska, *Geosphere*, *7*, 830–844, doi:10.1130/GES00654.1.

Sauber, J., B. Molnia, C. Carabajal, S. Luthcke, and R. Muskett (2005), Ice elevations and surface change on the Malaspina Glacier, Alaska, *Geophys. Res. Lett.*, *32*, L23S01, doi:10.1029/2005GL023943.

Scherler, D., D. Farinotti, R. S. Anderson, and M. R. Strecker (2010), Numerical modeling of a remote Himalayan glacier constrained by satellite data, *Geophys. Res. Abstr.*, *12*, EGU10494.

Sharp, R. P. (1951), Accumulation and ablation on the Seward-Malaspina glacier system Canada-Alaska, *Geol. Soc. Am. Bull.*, *62*(7), 725–744, doi:10.1130/0016-7606(1951)62[725:AAAOTS]2.0.CO;2.

Sheaf, M. A., L. Serpa, and T. L. Pavlis (2003), Exhumation rates in the St. Elias Mountains, Alaska, *Tectonophysics*, *367*(1–2), 1–11, doi:10.1016/S0040-1951(03)00124-0.

Shreve, R. L. (1972), Movement of water in glaciers, *J. Glaciol.*, *11*, 205–214.

Spotila, J. A., and A. L. Berger (2010), Exhumation at orogenic indentor corners under long-term glacial conditions: Example of the St. Elias orogen, Southern Alaska, *Tectonophysics*, *490*(3–4), 241–256, doi:10.1016/j.tecto.2010.05.015.

Spotila, J. A., J. T. Buscher, A. J. Meigs, and P. W. Reiners (2004), Long-term glacial erosion of active mountain belts: Example of the Chugach-St. Elias Range, Alaska, *Geology*, *32*(6), 501–504, doi:10.1130/G20343.1.

Tangborn, W. (1999), A mass balance model that uses low-altitude meteorological observations and the area-altitude distribution of a glacier, *Geogr. Ann., Ser. A*, *81*, 753–765, doi:10.1111/j.0435–3676.1999.00103.x.

Tomkin, J. H. (2007), Coupling glacial erosion and tectonics at active orogens: A numerical modeling study, *J. Geophys. Res.*, *112*, F02015, doi:10.1029/2005JF000332.

Tomkin, J. H., and J. Braun (2002), The influence of alpine glaciation on the relief of tectonically active mountain belts, *Am. J. Sci.*, *302*, 169–190, doi:10.2475/ajs.302.3.169.

Trusel, L. D., B. A. Willems, R. D. Powell, and L. A. Mayer (2008), Quantification of glacimarine sediment yields using multibeam sonar in Alaskan fjords, *Eos Trans. AGU*, *89*(53), Fall Meet. Suppl., Abstract C11B-0508.

Wobus, C. W., K. V. Hodges, and K. X. Whipple (2003), Has focused denudation sustained active thrusting at the Himalayan topographic front? *Geology*, *31*(10), 861, doi:10.1130/G19730.1.

Yanites, B. J., and T. A. Ehlers (2012), Global climate and tectonic controls on the denudation of glaciated mountains, *Earth Planet. Sci. Lett.*, *325–326*, 63–75, doi:10.1016/j.epsl.2012.01.030.

Zeitler, P. K., et al. (2001), Crustal reworking at Nanga Parbat, Pakistan: Metamorphic consequences of thermal-mechanical coupling facilitated by erosion, *Tectonics*, *20*(5), 712–728, doi:10.1029/2000TC001243.

Zhang, P. Z., et al. (2004), Continuous deformation of the Tibetan Plateau from global positioning system data, *Geology*, *32*(9), 809–812, doi:10.1130/G20554.1.